Light: Science & Applications (2013) 2, e94; doi:10.1038/lsa.2013.50
© 2013 CIOMP. All rights reserved 2047-7538/13
www.nature.com/lsa

ORIGINAL ARTICLE

Silicon micromirrors with three-dimensional curvature enabling lensless efficient coupling of free-space light

Yasser M Sabry[1,2], Bassam Saadany[2], Diaa Khalil[2,3] and Tarik Bourouina[1,2]

Miniaturized optical benches process free-space light propagating in-plane with respect to the substrate and have a large variety of applications, including the coupling of light through an optical fiber. High coupling efficiency is usually obtained using assembled micro-optical parts, which considerably increase the system cost and integration effort. In this work, we report a high coupling efficiency, monolithically integrated silicon micromirror with controlled three-dimensional (3D) curvature that is capable of manipulating optical beams propagating in the plane of the silicon substrate. Based on our theoretical modeling, a spherical micromirror with a microscale radius of curvature as small as twice the Gaussian beam Rayleigh range provides a 100% coupling efficiency over a relatively long optical path range. Introducing dimensionless parameters facilitates the elucidation of the role of key design parameters, including the mirror's radii of curvature, independent of the wavelength. A micromachining method is presented for fabricating the 3D micromirror using fluorinated gas plasmas. The measured coupling efficiency was greater than 50% over a 200-μm optical path, compared to less than 10% afforded by a conventional flat micromirror, which was in good agreement with the model. Using the 3D micromirror, an optical cavity was formed with a round-trip diffraction loss of less than 0.4%, resulting in one order of magnitude enhancement in the measured quality factor. A nearly 100% coupling was also estimated when matching the sagittal and tangential radii of curvature of the presented micromirror's surface. The reported class of 3D micromirrors may be an advantageous replacement for the optical lenses usually assembled in silicon photonics and optical benches by transforming them into real 3D monolithic systems while achieving wideband high coupling efficiency over submillimeter distances.
Light: Science & Applications (2013) **2,** e94; doi:10.1038/lsa.2013.50; published online 16 August 2013

Keywords: coupling efficiency; Gaussian beam coupling; micro-optics; monolithic chip; optical cavity; optical fabrication; optical benches; silicon photonics.

INTRODUCTION

Optical coupling is a critical performance feature in micro photonic components when considering either guided or free-space propagation of light. Guided wave coupling usually focuses on mode shapes, sizes and evanescent tails, and tapering;[1] diffraction grating[2] and proximity coupling[3] are typically used. By contrast, free-space coupling elements are usually designed to mitigate optical beam divergence phenomena associated with Gaussian beam (GB) propagation and achieve phase/mode matching.[4–23] Photonic applications in which the sources and destinations are separated by a free-space optical path (OP) such as fiber to fiber,[4] laser to fiber,[5–7] photonic crystal to fiber,[8] waveguide to fiber,[9–11] laser to laser[12–16] and intra chip coupling[17] have been reported. In many applications, a high coupling efficiency over a relatively long OP, within the submillimeter range and sometimes extending up to the centimeter range, is critical. For example, the coupling efficiency has a direct impact on the output power and tunable range of external cavity tunable lasers,[14] the finesse and free spectral range of Fabry-Pérot resonators[18] and the insertion loss and number of the input/output ports in optical switches,[19] as well as in optical interconnects.[17,20]

Micro lenses in the form of lens array,[19] ball lenses,[21] graded-index lenses[4,11] or lensed fibers[22] are the most commonly used optical components for focusing and matching GBs. The use of lenses, however, increases the system complexity and cost due to the required assembly process, a major obstacle to system integration. To the best of our knowledge, no three-dimensional (3D) monolithic microlens has been designed for micro optical benches (OBs); however, it is worth mentioning that several demonstrations of two-dimensional counterparts have been implemented based on surface-micromachined Fresnel lenses.[24–26] In addition to their inherent material absorption, optical lenses usually exhibit chromatic behavior due to material dispersion as well as the spectral response of their anti-reflective coating, which limits the system wavelength range. We therefore explore in this paper the potential of monolithically integrated silicon 3D micromirrors, which appear to be an efficient alternative to lenses for use in micro-OBs.

Silicon-based coupling micromirrors in both flat and cylindrical shapes have been reported.[13,23] The allowable OP was limited to tens of micrometers by the rapid decay of the coupling efficiency. This decay is caused by optical beam divergence, as shown in

[1]Université Paris-Est, ESYCOM (EA 2552), ESIEE Paris, F-93162 Noisy-le-Grand, France; [2]Si-Ware Systems, 3 Khaled Ibn El-Waleed Street, Heliopolis, Cairo 11361, Egypt and [3]Electron. and Comm. Eng. Dept., Faculty of Eng., Ain-Shams University, Cairo, Egypt
Correspondence: Dr T Bourouina, Université Paris-Est, ESYCOM (EA 2552), ESIEE Paris, F-93162 Noisy-le-Grand, France
E-mail: t.bourouina@esiee.fr
Received 14 October 2012; revised 17 January 2013; accepted 18 March 2013

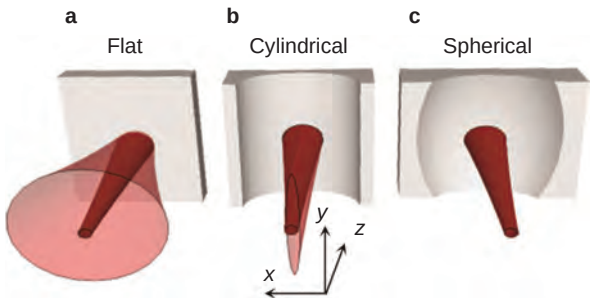

Figure 1 Impact of a micromirror's shape on GB reflection. (**a**) A flat mirror on which no focusing effect occurs on the reflected beam; (**b**) a cylindrical mirror on which the reflected beam can be focused in the tangential plane only; (**c**) a 3D spherical mirror on which full 3D focusing of the reflected beam can be achieved. 3D, three-dimensional; GB, Gaussian beam.

Figure 1a and 1b. Flat and cylindrical micromirrors can be easily obtained by a well-known microfabrication technique, Deep Reactive Ion Etching (DRIE), starting from photolithography-defined straight and curved patterns, respectively. Until now, high coupling efficiency with submillimeter OP in OBs has not been achieved without the assembly of a ball lens with flat mirrors,[12] the insertion of a fiber rod lens with cylindrical mirrors[14,15,18] or the hybrid integration of 3D mirrors, which requires further assembly or mounting steps.[24–28] In this work, we report on a monolithically integrated silicon 3D concave micromirror of controlled radii of curvature that is capable of focusing both the tangential and sagittal divergence of optical beams propagating in-plane of the substrate (x–z plane) as shown in Figure 1c.

MATERIALS AND METHODS

3D micromirror fabrication

The 3D spherical micromirrors were fabricated by a technique combining anisotropic DRIE, polymer (Teflon-like) formation on sidewalls and isotropic silicon etching technologies; the technique used was similar to that used to fabricate micro fluidic channels.[29] In our case, the processing etching steps all involved fluorinated gas plasmas. These technologies are compatible with and widely used for micro-optical device fabrication. The fabrication steps of the 3D micromirror are shown in Figure 2a. First, the in-plane profile of the micromirror was defined using standard photolithography (step 1) and SiO_2 as a mask material for the subsequent etching processes. Second, DRIE of the silicon was performed to yield a deeply etched cylindrical surface (step 2). This anisotropic etching step defined the optical axis of the desired 3D micromirror. The third fabrication step was a protective step for the previously etched sidewalls that involved the deposition of a polymer layer to prevent sidewall etching from both the top and side and to ensure the correct beginning of the following isotropic etching at the micromirror optical axis (step 3). The protective layer had to chemically and mechanically withstand the subsequent long etching step. A post-deposition bake of the polymer layer can improve its stability.[30] Alternatively, sidewall protection can be achieved using a layer of SiO_2 or SiN.[29] Fourth, a long isotropic etching was used to achieve the desired out-of-plane curved profile of the micromirror (step 4). In our case, the out-of-plane profile was given special attention to achieve a curved profile with a relatively large radius of curvature to satisfy the requirements of the desired optical design. This was achieved through optimization steps for tuning the isotropic etching recipe and time. A detailed discussion of the dry isotropic etching of silicon using sulfur hexafluoride (SF_6) and the effect of different process parameters on the resulting surface quality can be found in Refs. 31 and 32. The scanning electron microscope (SEM) images shown in Figure 2b and 2c show an example of a resulting structure after etching completion. The presented micromirror can also serve as a cylindrical micromirror if the beam axis lies within the top part of the micromirror.

For optical surface quality, a post-etching smoothing process using a mixture of hydrofluoric, nitric and acetic acids was required (step 5 in Figure 2a). The polishing process had to be sufficiently uniform to smooth the micromirror surface without changing its curvature in both planes. This was achieved through the use of appropriate acid concentrations and volumetric amounts with continuous stirring of the solution.[33] SEM images of the micromirror surface before and after smoothing are shown in Figure 2d; the improvement of the surface quality is clearly visible. The peak-to-peak roughness measured by SEM after 15 min of smoothing is less than 50 nm, compared to more than 300 nm before smoothing. Finally, the micromirror surface was coated with an aluminum layer using the metal sputtering technique. This step can be performed through a shadow mask to protect parts from metallization, if necessary.[34–36] The resulting Al layer has a thickness of nearly 100 nm to maintain high optical reflectivity with wide spectral bandwidth.[37] The mirror reflectivity was measured at 675 nm and 1550 nm wavelengths and found to be larger than 92%, which indicates a high-quality optical surface.

The presented method is versatile enough to obtain a wide range of curvature radii suitable for micro-OBs. Using a single crystal silicon substrate, out-of-plane radii of curvature ranging from 30 μm and up to 200 μm were achieved. The maximum obtainable value was limited by the substrate thickness, which is normally approximately 500 μm. Larger radii of curvature could be obtained by increasing the isotropic etching time, but increasing the etching time might lead to a fragile wafer that is subject to breakage in the etching reactor. By using silicon on insulator (SOI) wafers instead, the buried oxide layer acts as an etch-stop layer and larger radii of curvature can be obtained without further deep etching of the wafer substrate.[36] The principle of this method was evaluated on a SOI wafer using ELITE, an advanced simulator within the ATHENA process simulation framework provided by SILVACO, Inc. (Santa CA, California, USA). Out-of-plane radii of curvature larger than 500 μm were achievable. Interestingly, even with 100–200 μm radii of curvature, the fabricated 3D micromirror achieved efficient power coupling, as will be shown in the results and discussion section. Indeed, several micro-OBs with comparable optical paths have been reported in the literature in which integrating the 3D micromirror would reduce the optical losses or overcome the need for lensed fibers.[13–16,18,38–41] It is also possible to incorporate multiple 3D mirrors with different radii of curvature on the same SOI substrate. The latter can be implemented either by exploiting the RIE-lag effect[36] or by the sequential application of the presented method while protecting the already-etched mirrors by the sidewall protection technique mentioned previously.

Rendering the 3D micromirror movable adds another dimension to its applications. A schematic of an SOI OB monolithically accommodating a 3D micromirror of the presented class as well as other flat-surface devices that are usually fabricated by conventional DRIE is shown in Figure 2e. The optical axis depth of the fabricated 3D micromirror with respect to the wafer top surface can be sufficiently large such that an optical fiber or other compatible sources can be inserted into a groove and aligned with the 3D micromirror for optical beam injection/extraction. The 3D micromirror can be freestanding and attached to a MEMS actuator such as a comb-drive by etching the

doi:10.1038/lsa.2013.50

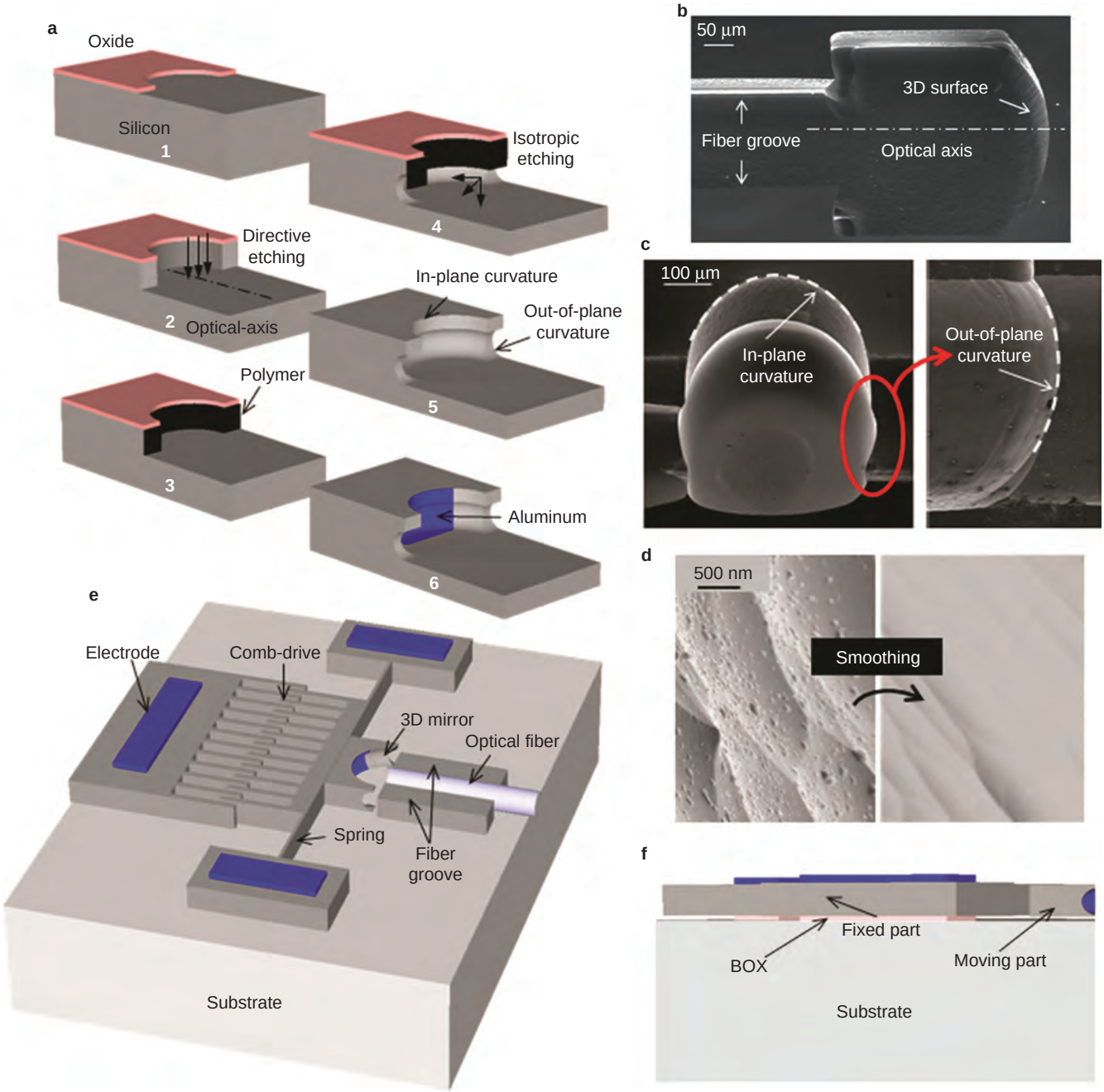

Figure 2 (**a**) 3D spherical micromirror fabrication steps. (**b**) A SEM image for a fabricated fiber groove/3D mirror structure. (**c**) SEM images focused on the fabricated 3D micromirror in which the achieved out-of-plane and in-plane radii of curvature are approximately 100 μm and 200 μm, respectively. The effect of post-etching smoothing is shown in (**d**), where the peak-to-peak roughness is reduced sixfold. (**e**) A schematic illustration of possible extension leading to an SOI optical bench containing the presented 3D mirror monolithically integrated with a MEMS actuator and a fiber groove. (**f**) A side view of the moving parts with the sacrificial BOX layer etched while the fixed parts remain anchored. BOX, buried oxide; 3D, three-dimensional; SEM, scanning electron microscope; SOI, silicon on insulator.

sacrificial buried oxide layer (Figure 2f) of the SOI wafer underneath the micromirror using the standard release methods.[42] Indeed, the monolithic addition of the presented 3D micromirrors to the OB changes its nature from a quasi 3D to a real 3D system. Generally, the OB may show a higher degree of complexity by monolithic integration of more than one 3D micromirror, which allows the light to traverse relatively long optical paths in between the micromirrors without suffering from high propagation loss, as well as efficient coupling into the final destination.

Optical measurements

The optical performance of the presented class of micromirrors was experimentally tested for a fabricated 3D micromirror having in-plane and out-of-plane radii of curvature of 200 μm and 100 μm, respectively. A single-mode (SM) cleaved optical fiber fed from a semiconductor laser source was used to generate the GB incident on the micromirror. A Thorlabs S1FC675 Fabry-Perot laser source and an Agilent 81662A distributed feedback laser source were used at wavelengths of 675 nm and 1550 nm, respectively. A standard SM fiber with

a core radius of 4.5 μm and a special SM fiber with a core radius of 2 μm were utilized to generate the beams at 1550 nm and 675 nm, respectively. The fabricated 3D micromirror was used to couple back the GB into the fiber as illustrated in the coupling configuration shown in Figure 2a by inserting the optical fiber in the etched groove facing the 3D micromirror. The power coupled back was separated by means of a Directional Coupler (DC) and measured by an optical Power Meter (PM) as schematically shown in Figure 3. The experiment was conducted at wavelengths of 1550 nm and 675 nm by exploiting the wide spectral response of the micromirror coupling. Special attention was given to the process of aligning the optical fiber with respect to the mirror optical axis to avoid misalignment coupling losses, which will be discussed in the theoretical analysis section. This alignment process can be conducted more easily if a fiber groove matching the optical fiber size is used. For the sake of comparison, in addition to the 3D micromirror, flat as well as cylindrical micromirrors were fabricated using standard DRIE and measured. The distance between the fiber cleaved surface and the micromirror surface was varied, and the power coupled back was recorded. In another experiment, a SM fiber cleaved surface with a multilayer dielectric coating was used to form an optical cavity with the 3D micromirror, making use of its efficient coupling capability. The fiber surface has a reflectivity of approximately 98% at 1330 nm and decreases rapidly away from this wavelength. The fiber was fed from a Super Luminescent Diode (SLD) with a central wavelength of 1330 nm, and the power returned from the directional coupler was monitored on an Optical Spectrum Analyzer (OSA).

RESULTS AND DISCUSSION

Theoretical analysis

The field coupling between the normalized incident beam and the beam reflected back by the mirror, as shown in Figure 1, can be calculated using the following overlap integral:[43,44]

$$k=\iint E_i E_r^* \mathrm{d}A=\frac{2j\lambda}{\pi}\left[w_{it}w_{is}w_{rt}w_{rs}\left(\frac{1}{q_{it}^*}-\frac{1}{q_{rt}}\right)\left(\frac{1}{q_{is}^*}-\frac{1}{q_{rs}}\right)\right]^{-0.5} \quad (1)$$

where the subscripts i and r stand for the incident and reflected GBs, respectively, λ is the wavelength, w is the GB spot radius, q is the GB complex phase radius of curvature and the subscripts t and s refer to the tangential and sagittal planes, respectively. The incident and reflected GBs can be related to each other by two different **ABCD** matrices, corresponding to the tangential and sagittal planes. Noting that the incident GB parameters are given by $w=w_o$ and $q=jz_o=j\pi w_o^2/\lambda$ and that the **ABCD** matrix parameters satisfy the relation AD−BC=1, it can be proven that the power coupling efficiency between the two beams can be expressed by:

$$\eta=|k|^2=\frac{4z_{ot}z_{os}}{\sqrt{B_t^2+z_{ot}^2\left(A_t^2+D_t^2+2\right)+z_{ot}^4C_t^2}\sqrt{B_s^2+z_{os}^2\left(A_s^2+D_s^2+2\right)+z_{os}^4C_s^2}} \quad (2)$$

where w_o is the beam min spot radius and z_o is the GB Rayleigh range. The expression in Equation (2) can be generally used to calculate the coupling efficiency in OBs once their **ABCD** matrices are known. It will be used hereinafter to study the coupling configurations in Figure 4 when the 3D spherical mirror has a microscale radius of curvature, i.e., comparable to the optical beam Rayleigh range. The elements of the **ABCD** matrices can be easily derived considering the mirror radius of curvature R and the propagation distances d, d_1 and d_2.

For the single-mirror coupling configuration shown in Figure 4a and 4c, Equation (2) is reduced to the following:

$$\eta=\left[0.5+\left(\frac{d}{z_o}\right)^2\left(1-\frac{d}{R}\right)^2+0.5\left(1-\frac{2d}{R}\right)^2+\left(\frac{z_o}{R}\right)^2\right]^{-1} \quad (3)$$

The coupling efficiency behavior versus the dimensionless distance ratio d/z_o at $z_o/R=2$, 1, 0.5, 0.25 and 0.125 is depicted in Figure 5a. For $z_o/R=2$ or 1, the maximum achievable coupling efficiency is much smaller than 100%. Full coupling can be achieved only when $z_o/R\leqslant 0.5$. The specific case of $z_o/R=0.5$ has a unique flat response centered on $d/z_o=1$. The 1 dB width of the response extends from zero up to $d/z_o=2$. Indeed, this response is very convenient for implementing a wide tuning mechanism involving, for instance, MEMS actuators for the mirror position centered on $d/z_o=1$, leading to a nearly flat maximal response over a distance $\Delta d=\pm z_o$. This is of particular interest for applications such as optical delay lines and external cavity tunable lasers. For $z_o/R<0.5$, two full-coupling extremes exist in which the first one is located close to zero while the second one is close to $d=R$. The location of the second peak becomes weakly dependent on z_o for smaller z_o/R ratios. In such a situation, the spherical micromirror possesses the capability of efficiently coupling both elliptical as

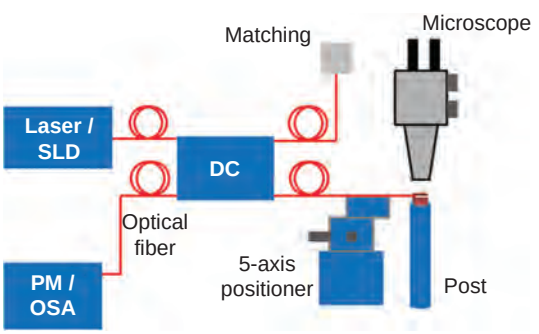

Figure 3 Schematic drawing of the experimental set-up.

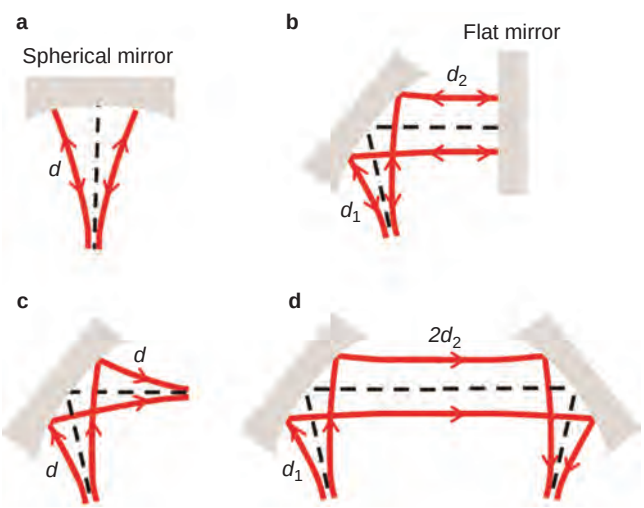

Figure 4 Spherical micromirrors used in configurations (**a**) and (**b**) for coupling back the beam to its source and in configurations (**c**) and (**d**) for coupling the beam from a source to a destination.

doi:10.1038/lsa.2013.50

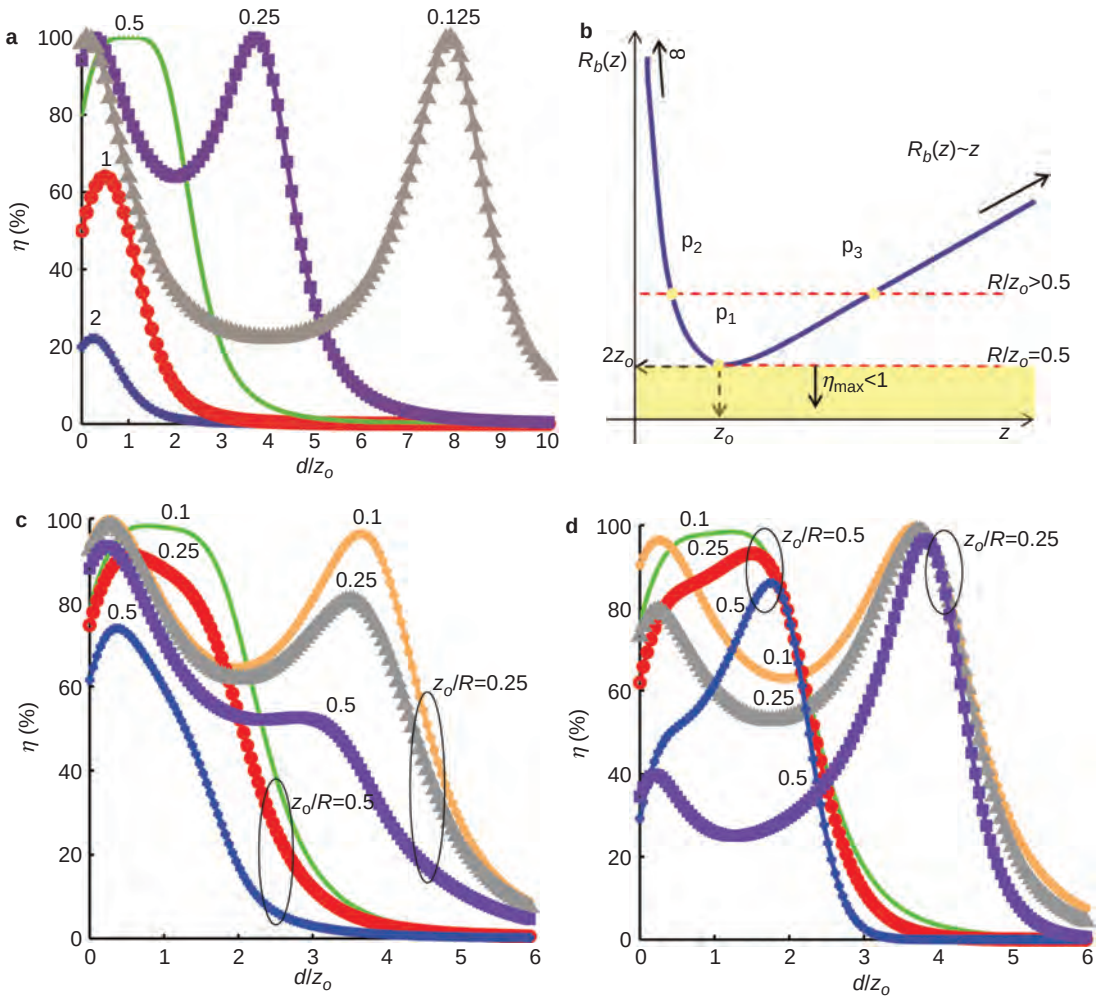

Figure 5 (**a**) The power coupling efficiency of a single spherical mirror versus the dimensionless distance ratio d/z_o at different values of the ratio z_o/R. (**b**) The coupling behavior is related to the GB phase radius of curvature R_b versus the distance to beam waist z. The effect of the misalignment between the incident GB and the 3D mirror optical axes on the power coupling efficiency: the effect of shift misalignment is shown in (**c**) for δ/w_o ratios of 0.1, 0.25 and 0.5 at z_o/R=0.25 and 0.5, while the effect of rotational misalignment is shown in (**d**) for β/θ_{div} ratios of 0.1, 0.25 and 0.5. 3D, three-dimensional; GB, Gaussian beam.

well as circular beams for a relatively wide wavelength range. Elliptical GBs are typical outputs of semiconductor lasers, while the efficient coupling of a wide-bandwidth optical source output is mandatory in low coherence applications.

The encountered behavior related to the ratio z_o/R can be explained as follows. For perfect beam focusing, the mirror radius of curvature should match the incident GB phase radius of curvature R_b, where the latter exhibits the dependence shown in Figure 5b on the distance z to the beam waist. The minimum phase radius is twice the GB Rayleigh range (R_b=2z_o). If the mirror radius of curvature is smaller than 2z_o, the maximum achievable coupling will be always smaller than 100%, posing a single extreme value and preventing high coupling over a long distance. This extreme becomes closer to 100% and its location approaches z_o when the mirror radius of curvature approaches 2z_o (see point p_1). When the mirror radius of curvature is greater than 2z_o, a full-coupling condition can be satisfied at two different locations simultaneously (see points p_2 and p_3), before and after the location where z=z_o. As the mirror radius of curvature becomes larger, the first of these locations approaches zero, while the second location becomes approximately equal to the mirror radius of curvature.

In some practical situations, slight misalignment may arise between the optical axes of the incident GB and the spherical mirror or the optical system in general. This can result in a lateral shift Δ and/or angular shift α between the incident and the coupled back GBs. Consequently, the power coupling efficiency will be reduced. In this case, it can be proven that the coupling efficiency derived in Equation (2) will be modified to the following:

$$\eta_{\mathrm{mis}} = \eta \exp\left[\frac{-2\pi\Delta^2 z_o(1+D^2)+C^2 z_o^3}{\lambda[B^2+z_o^2(A^2+D^2+2)+z_o^4C^2]}\right] \exp\left[-\frac{2\pi\alpha^2 z_o\left(B^2+A^2z_o^2\right)}{\lambda\left(B^2+A^2z_o^2+z_o^2\right)}\right] \quad (4)$$

where η_{mis} is the coupling efficiency in case of misalignment and A, B, C and D are the matrix elements for the plane in which the misalignment occurs. A simulation study was performed in which the incident beam optical axis was shifted by δ or rotated by β with respect to the optical axis of the spherical mirror, as shown in Figure 3a. The corresponding lateral and angular shift between the incident and the coupled back GB were deduced from the geometry of the problem.

The results are depicted in Figure 5c for δ/w_o=0.1, 0.25 and 0.5 and in Figure 5d for β/θ_{div}=0.1, 0.25 and 0.5, where θ_{div} is the divergence half-angle of the GB. For z_o/R=0.25, the impact of shift misalignments is insignificant within the first peak of the coupling curve due to the small distance between the mirror and GB waist location. A similar impact is encountered in the case of rotational misalignments within the second peak of the coupling curve because the GB waist is in close proximity to the mirror center. Considering the case of z_o/R=0.5, as if being composed of two overlapping peaks, a similar insight can be gained. In effect, misalignment ratios on the order of 0.1–0.2 cause a small coupling loss that can be tolerated in many optical systems. These ratios can be translated to 1 μm/(°) misalignments for a GB waist w_o=5 μm at a wavelength of 1550 nm. To tolerate larger misalignments, an active alignment technique should be applied.[45]

For the double-mirror coupling configurations shown in Figure 4b and 4d, full coupling is achieved when $d_1=R/2$ and $d_2=R/2$ such that the beam in-between the mirrors is maintained with minimum divergence and the beam phase curvature is matched by the second reflecting mirror. For $d_2=R/2$, Equation (2) is reduced to the following:

$$\eta=\left[1+\left(\frac{d_1-R/2}{z_o}\right)^2\right]^{-1} \tag{5}$$

The coupling behavior versus the ratio d_1/z_o at z_o/R=2, 1, 0.5, 0.25 and 0.125 is depicted in Figure 6a. In contrast to the single-mirror coupling configuration, full coupling can be achieved for any ratio of z_o/R using this configuration. There is a single peak located at $d_1=R/2$ with 1 and 3 dB widths of approximately $\Delta d=\pm 0.5z_o$ and $\pm 0.5z_o$, respectively, independent of the ratio z_o/R. By contrast, for $d_1=R/2$, Equation (2) is reduced to the following:

$$\eta=\left[1+4\left(\frac{z_o}{R}\right)^2\left(1-\frac{2d_2}{R}\right)^2\right]^{-1} \tag{6}$$

The coupling behavior versus the ratio d_2/z_o at z_o/R=2, 1, 0.5, 0.25 and 0.125 is depicted in Figure 6b. Again, there is a single peak located at $d_2=R/2$, and it becomes flatter and wider for smaller z_o/R ratios. Thus, for $z_o/R\geqslant 0.5$, full coupling in the single- and double-mirror coupling configurations occurs when d or $d_2=R/2$, with a wider response in the single-mirror configuration. For $z_o/R<0.5$, the single-mirror configuration offers two full-coupling locations, each with a narrower response than the double-mirror configuration. For example, the 1 dB width of the response extends from zero up to d_2/z_o=12 when z_o/R=0.125. Practical limits arise due to the need for precise alignment between the source, the two mirrors and the destination.

Coupling efficiency

The ratio between the SM fiber GB Rayleigh range at 1550 nm and the presented 3D micromirror's out-of-plane radius of curvature is approximately 0.5. For this reason, the micromirror was used in the coupling configuration as shown in Figure 2a. The micromirror under investigation, which has unmatched radii of curvature of 100 μm and 200 μm, is expected to have a more realistic coupling efficiency profile with respect to those presented in the theoretical analysis section. In this case, Equation (2) is reduced to the following:

$$\eta=\left[0.5+\left(\frac{d}{z_o}\right)^2\left(1-\frac{d}{R_i}\right)^2+0.5\left(1-\frac{2d}{R_i}\right)^2+\left(\frac{z_o}{R_i}\right)^2\right]^{-0.5}\left[0.5+\left(\frac{d}{z_o}\right)^2\left(1-\frac{d}{R_o}\right)^2+0.5\left(1-\frac{2d}{R_o}\right)^2+\left(\frac{z_o}{R_o}\right)^2\right]^{-0.5} \tag{7}$$

where R_i and R_o are the in-plane and out-of-plane radii of curvature, respectively. The measured power coupling efficiencies for the fabricated micromirrors are depicted in Figure 7a and 7c at 675 nm and 1550 nm, respectively. The corresponding theoretical results expected from equation (7) are depicted in Figure 7b and 7d, in which a good correspondence between the model and the experimental results can be observed. A significant improvement in the power coupling efficiency is introduced by the use of the presented 3D micromirror compared to flat or cylindrical micromirrors. For an optical path of 200 μm (i.e., d=100 μm), the power coupling efficiencies are approximately 15%, 32% and 60% for the flat, the cylindrical and the presented 3D micromirrors, respectively, indicating a 6 dB improvement at 1550 nm over flat mirrors. At 675 nm, the power coupling efficiencies are approximately 10%, 18% and 52%, indicating a 7 dB improvement. A fast roll-off at 675 nm in the efficiency response with distance can be observed for the flat micromirror, while a small hump near 270 μm occurs in the case of the cylindrical micromirror due to GB focusing in the tangential direction. A slower roll-off is observed for the 3D micromirror, and double humps exist near 180 μm and 370 μm,

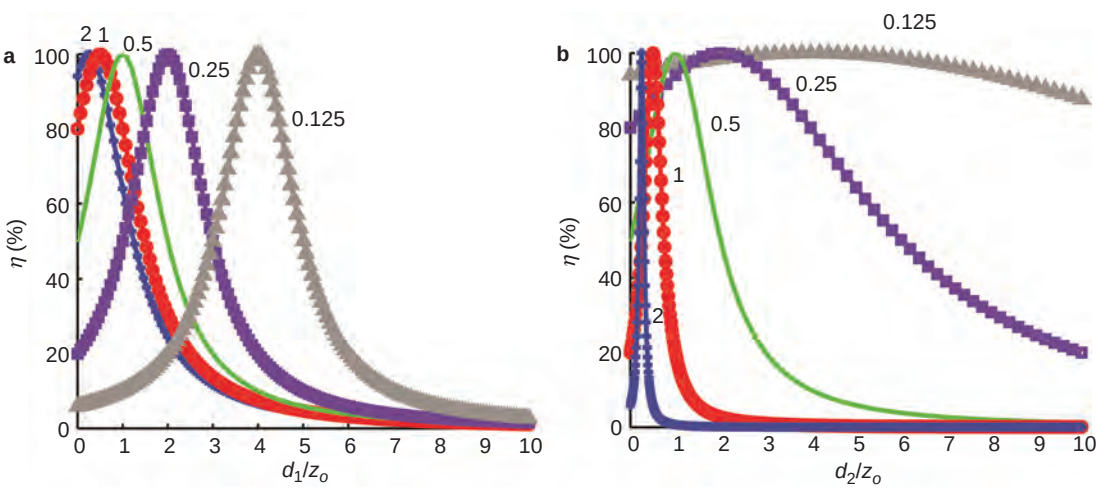

Figure 6 Power coupling efficiency using two spherical mirrors versus the ratio d_1/z_o for $d_2=R/2$ in (**a**) and versus d_2/z_o for $d_1=R/2$ in (**b**), at different z_o/R ratios.

doi:10.1038/lsa.2013.50

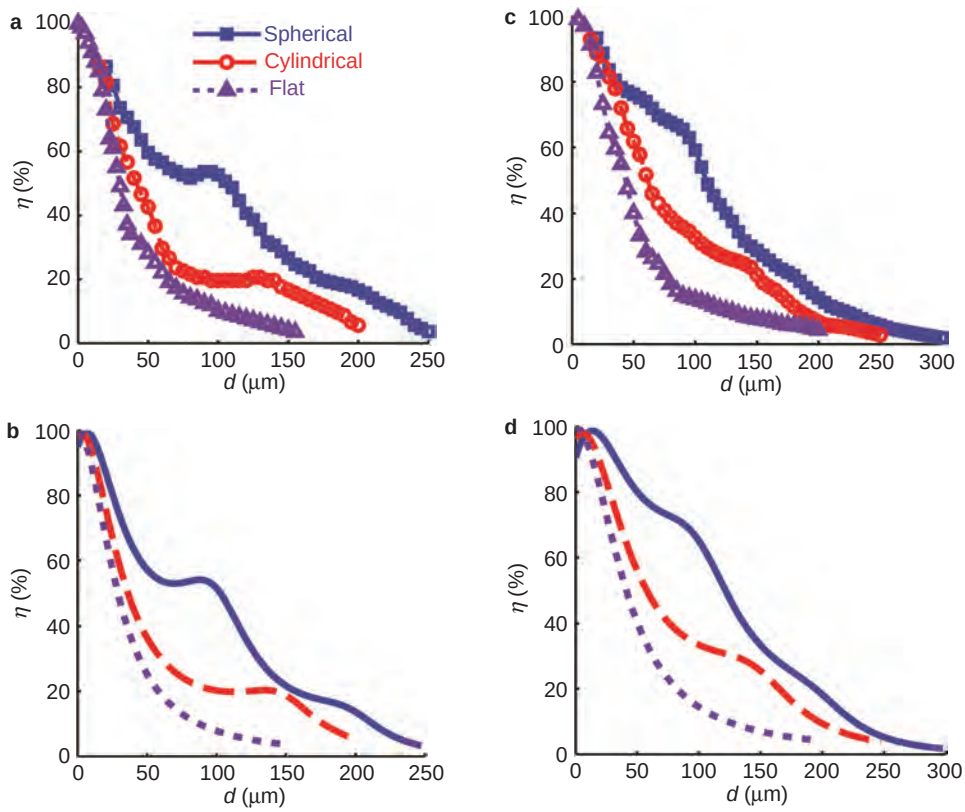

Figure 7 Measured power coupling efficiency of the presented 3D spherical micromirror with an in-plane radius of curvature of 200 μm and an out-of-plane radius of curvature of 100 μm. For reference, the power coupling efficiencies were also measured on a cylindrical micromirror with an in-plane radius of curvature of 150 μm and on a flat micromirror. The coupling efficiency is depicted in (**a**) for measurements performed at a wavelength of 675 nm and in (**c**) for measurements performed at a wavelength of 1550 nm. Their corresponding theoretical model data are depicted in (**b**) and (**d**), respectively. 3D, three-dimensional.

due to the unequal radii of curvature of the micromirror and the associated GB focusing in the sagittal and tangential planes, respectively. These humps are more distinct at 675 nm due to the smaller z_o/R ratio. Indeed, using the 3 dB coupling distance as a performance indicator, the presented 3D micromirror can improve the coupling distance by approximately 2.5- and 3.5-fold at 1550 nm and 675 nm, respectively. Note that the presented 3D micromirror has an engineered coupling efficiency response with respect to a spherical mirror of matched radii of curvature. Therefore, although the micromirror did not achieve 100% coupling efficiency, the resulting profile does not drop drastically from its high coupling humps, as in the case of a micromirror with matched radii of curvature shown in Figure 5a.

Optical cavity

Exploiting its high coupling efficiency, the presented 3D micromirror was used to form a Fabry-Perot cavity. The cavity reflecting surfaces are formed from the metalized surface of the 3D mirror and the multilayer-coated cleaved-surface of a SM fiber inserted into the groove facing the mirror. In this manner, light can be trapped in the cavity while propagating in-plane with respect to the substrate. To demonstrate the multi-wavelength coupling property of the mirror, the cavity response was measured at approximately 1330 nm. The response was extracted by first measuring the power spectral density of the super luminescent diode source and then normalizing the cavity response with respect to the super luminescent diode. The cavity length was adjusted to obtain a narrow notch in the measured reflection response, yielding a free spectral range of approximately 26 nm, as shown in Figure 8a, with a corresponding cavity length of approximately 33 μm. The notch at 1333 nm is narrower than the preceding notch at 1307 nm because of the lower reflectivity of the fiber coating at lower wavelengths. An expansion of the sharp notch complimentary response is shown in Figure 8b. The obtained response has a line width that is slightly smaller than 0.45 nm, demonstrating a quality factor of approximately 3000 for the formed cavity. For the sake of comparison, the cavity was formed once again using a flat micromirror. The measured reflection response is shown in Figure 8c; the line width calculation is shown in Figure 8d. In this case, the contrast of the response at approximately 1330 nm is very low due to the encountered diffraction loss, which causes a significant mismatch between the power returned from the cavity to the fiber and the power reflected from the fiber end face.[46] The line width of the flat micromirror cavity is approximately 6 nm, which is approximately 13 times worse than the line width obtained with the 3D micromirror. Given that the reflectivities of the coated fiber and the metalized mirror are 0.98 and 0.92, respectively, the round-trip coupling of the 3D micromirror was estimated to be approximately 0.996 for a quality factor of 3000. Therefore, the obtained cavity performance is relatively diffraction-loss free and mainly limited by the mirror's reflectivity, which can be improved. In addition, optimization of the spherical mirror radii of curvature will further reduce the diffraction loss, potentially leading to order(s) of magnitude improvement in the quality factor.

CONCLUSION

A monolithically integrated 3D micromirror was demonstrated to achieve wideband efficient coupling of light over a submillimeter

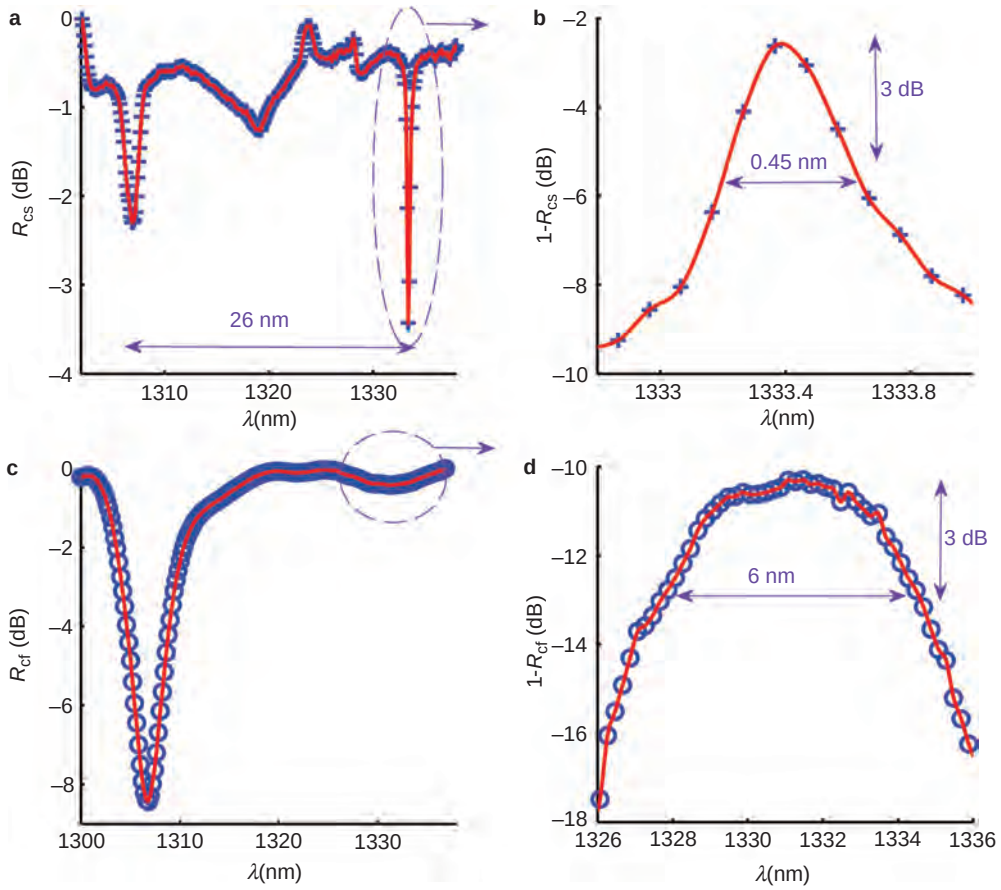

Figure 8 Measured reflection spectral response of the coated fiber-mirror cavity. The response using the presented 3D micromirror is shown in (**a**) with a free spectral range of approximately 26 nm; a corresponding line width of 0.45 nm could be obtained as calculated in (**b**). The response using a flat micromirror is shown in (**c**); the corresponding line width is approximately 6 nm as shown in (**d**). The 3D micromirror enhanced the quality factor by more than one order of magnitude. 3D, three-dimensional.

optical path without the need for additional lens assembly. The micromirror wavelength range has the advantage of being unlimited by material absorption and AR coating, in contrast to micro lenses. The micromirror also permits the manipulation of stigmatic and astigmatic beams over a wide wavelength range. In our study, normalization with respect to the GB Rayleigh range was conducted such that the results were independent of the specific values of the beam parameters and wavelength. Spherical micromirrors were found to be suitable for GB coupling at a mirror radius of curvature $R \geqslant 2z_o$ (the GB Rayleigh range). In this case, the spherical micromirrors can provide an almost 100% coupling efficiency, with the potential for use in tunable devices, enabling high coupling efficiency over the wide tuning range of the optical path, even with small spot sizes. A micromachining method was presented to fabricate 3D metalized micromirrors with controlled and independent radii of curvature in two orthogonal planes. The micromirror is capable of manipulating an optical beam propagating in-plane with respect to the substrate. The presented class of 3D micromirrors can be monolithically integrated with silicon OBs rendering the latter real 3D microsystems. A 3D micromirror with in-plane and out-of-plane radii of curvature of 200 μm and 100 μm, respectively, was fabricated, and its optical performance was measured. The 3D micromirror was used to couple back the GB of single-mode fibers at wavelengths of 675 nm and 1550 nm, exploiting its wide spectral response. The 3 dB optical path was increased 2.5- and 3.5-fold at 1550 nm and 675 nm, respectively, compared to a flat micromirror fabricated using conventional DRIE technology. An optical cavity was formed from a multilayer-coated cleaved-surface SM fiber inserted into a groove facing the 3D micromirror, causing light to be trapped inside the cavity while propagating in-plane of the wafer substrate. The measured cavity line width is 0.45 nm at an approximate wavelength of 1330 nm, indicating an obtained quality factor close to 3000 and offering a greater than one order of magnitude enhancement over a flat micromirror cavity.

ACKNOWLEDGMENTS

This work was partially supported by the Information Technology Industry Development Agency (ITIDA) through the ITAC program.

1 Bienstman P, Assefa S, Johnson SG, Joannopoulos JD, Petrich GS *et al*. Taper structures for coupling into photonic crystal slab waveguides. *JOSA B* 2003; **20**: 1817–1821.
2 Roelkens G, Vermeulen D, Laere FV, Selvaraja S, Scheerlinck S *et al*. Bridging the gap between nanophotonic waveguide circuits and single mode optical fibers using diffractive grating structures. *J Nanosci Nanotechnol* 2010; **10**: 1551–1562.
3 Meinzer N, Konig M, Ruther M, Linden S, Khitrova G *et al*. Distance-dependence of the coupling between split-ring resonators and single-quantum-well gain. *App Phys Lett* 2011; **99**: 111104-1–111104-3.
4 Zickar M, Noell W, Marxer C, de Rooij N. MEMS compatible micro-GRIN lenses for fiber to chip coupling of light. *Opt Express* 2006; **14**: 4237–4249.
5 Presby HM, Benner AF, Edwards CA. Laser micromachining of efficient fiber microlenses. *Appl Opt* 1990; **29**: 2692–2695.

doi:10.1038/lsa.2013.50

6 Edwards CA, Presby HM, Dragone C. Ideal microlenses for laser to fiber coupling. *IEEE J Lightw Technol* 1993; **11**: 252–257.
7 Thual M, Chanclou P, Gautreau O, Caledec L, Guignard C *et al*. Appropriate micro-lens to improve coupling between laser diodes and singlemode fibres. *Electron Lett* 2003; **39**: 1504–1506.
8 Liu L, Pu M, Yvind K, Hvam JM. High-efficiency, large-bandwidth silicon-on-insulator grating coupler based on a fully etched photonic crystal structure. *App Phys Lett* 2010; **96**: 051126–051128.
9 Wang Q, Loh TH, Ng KT, Ho ST. Design and analysis of optical coupling between silicon nanophotonics waveguide and standard single-mode fiber using an integrated asymmetric Super-GRIN lens. *IEEE J Sel Top Quant Electron* 2011; **17**: 581–589.
10 Kopp C, Bernabé S, Ben Bakir B, Fedeli JM, Orobtchouk R *et al*. Silicon photonic circuits: on-CMOS integration, fiber optical coupling, and packaging. *IEEE J Sel Top Quant Electron* 2010; **17**: 498–509.
11 Loh TH, Wang Q, Zhu J, Ng KT, Lai YC *et al*. Ultra-compact multilayer Si/SiO_2 GRIN lens mode-size converter for coupling single-mode fiber to Si-wire waveguide. *Opt Express* 2010; **18**: 21519–21533.
12 Syms RR, Lohmann A. MOEMS tuning element for a Littrow external cavity laser. *J Microelectromech S* 2003; **12**: 921–928.
13 Zhang XM, Liu AQ, Tang DY, Lu C. Discrete wavelength tunable laser using microelectromechanical systems technology. *Appl Phys Lett* 2004; **84**: 329–331.
14 Liu AQ, Zhang XM. A review of MEMS external-cavity tunable lasers. *J Micromech Microeng* 2007; **17**: R1.
15 Geerlings E, Rattunde M, Schmitz J, Kaufel G, Wagner J *et al*. Widely tunable micro-mechanical external-cavity diode laser emitting approximately 2.1 μm. *IEEE J Quantum Electron* 2008; **44**: 1071–1075.
16 Tao JF, Yu AB, Cai H, Zhu WM, Zhang QX *et al*. Ultra-high coupling efficiency of MEMS tunable laser *via* 3-dimensional micro-optical coupling system. In: Proceedings of the 24th IEEE International Conference on MEMS; 23–27 January 2011; Cancun, Mexico. IEEE: New York, USA, pp11–13.
17 Miller D. Device requirements for optical interconnects to silicon chips. *Proc IEEE* 2009; **97**: 1166–1185.
18 Malak M, Pavy N, Marty F, Peter YA, Liu AQ *et al*. Micromachined Fabry–Perot resonator combining submillimeter cavity length and high quality factor. *App Phys Lett* 2011; **98**: 211113-1–211113-3.
19 Yano M, Yamagishi F, Tsuda T. Optical MEMS for photonic switching-compact and stable optical crossconnect switches for simple, fast, and flexible wavelength applications in recent photonic networks. *IEEE J Sel Top Quant Electron* 2005; **11**: 383–394.
20 Heming R, Wittig LC, Dannberg P, Jahns J, Kley EB *et al*. Efficient planar-integrated free-space optical interconnects fabricated by a combination of binary and analog lithography. *IEEE/OSA J Lightw Technol* 2008; **26**: 2136–2141.
21 Lee SS, Huang LS, Kim CJ, Wu MC. Free-space fiber-optic switches based on MEMS vertical torsion mirrors. *IEEE/OSA J Lightw Technol* 1999; **17**: 7–13.
22 Bashir A, Katila P, Ogier N, Saadany B, Khalil DA. A MEMS-based VOA with very low PDL. *IEEE Photon Technol Lett* 2004; **16**: 1047–1049.
23 Uenishi Y, Honma K, Nagaoka S. Tunable laser diode using a nickel micromachined external mirror. *IEEE Electron Lett* 1996; **32**: 1207–1208.
24 Wu MC, Lin LY, Lee SS, Pister KS. Micromachined freespace integrated micro-optics. *Sens Actuators* 1995; **50**: 127–134.
25 Lee SS, Lin LY, Wu MC. Surface-micromachined free-space micro-optical systems containing three-dimensional microgratings. *App Phys Lett* 1995; **67**: 2135–2137.
26 Lin LY, Shen JL, Lee SS, Wu MC. Surface-micromachined micro-*xyz* stages for free-space micro-optical bench. *IEEE Photonic Tech Lett* 1997; **9**: 345–347.
27 Flanders DC, Whitney PS, Masghati M, Racz LM. Mounting and alignment structures for optical components. US patent 6,625,372. 2003 Sep 23.
28 Do K, Sell JE, Kono R, Jones DS, de la Torro R *et al*. Micro optical bench for mounting precision alighned optics, optical assembly and method of mounting optics. US patent 6,775,076. 2004 Aug 10.
29 de Boer MJ, Tjerkstra RW, Berenschot JW, Jansen HG, Burger GJ *et al*. Micro-machining of buried micro channels in silicon. *IEEE/ASME J Microelectromech Syst* 2000; **9**: 94–103.
30 Gaugel DM. CMOS-compatible fluidic chip cooling using buried channel technology. MSc thesis, Carnegie Mellon University, Pittsburgh, PA, USA, 2001.
31 Zhu X, Greve DW, Fedder GK. Characterization of silicon isotropic etch by inductively coupled plasma etch in post-CMOS processing. In: Proceedings of the 13th IEEE Annual Conference on Micro Electro Mechanical Systems; 20–24 January Taipei, Taiwan. IEEE: New York, USA, 2000, pp568–573.
32 Larsen KP, Petersen DH, Hansen O. Study of the roughness in a photoresist masked isotropic SF_6-based ICP silicon etch. *J Electrochem Soc* 2006; **153**: G1051–G1058.
33 Moktadir Z, Koukharenka E, Kraft M, Bagnall DM, Powell H *et al*. Etching techniques for realizing optical micro-cavity atom traps on silicon. *J Micromech Microeng* 2004; **14**: S82.
34 Cowen A, Hames G, Monk D, Wilcenski S, Hardy B. *SOIMUMPS Design Handbook*. Vol. 6. Research Triangle Park, NC: MEMSCAP; 2009.
35 Saadany B, Diaa K, Tarik B. System, method and apparatus for a micromachined interferometer using optical splitting. US patent 7796267. 2010 Sep 14.
36 Sabry Y, Tarik B, Saadany B, Diaa K. Integrated monolithic optical bench containing 3-D curved optical elements and methods of its fabrication. US patent application 1261078. 2013 Apr 25.
37 Bartl J, Baranek M. Emissivity of aluminium and its importance for radiometric measurement. *Meas Phys Quant* 2004; **4**: 31–36.
38 Li J, Zhang QX, Liu AQ. Advanced fiber optical switches using deep RIE (DRIE) fabrication. *Sensor Actuat A* 2003; **102**: 286–295.
39 Saadany B, Malak M, Kubota M, Marty F, Mita Y *et al*. Free-space tunable and drop optical filters using vertical Bragg mirrors on silicon. *IEEE J Sel Top Quant Electron* 2006; **12**: 1480–1488.
40 Lim TS, Ji CH, Oh CH, Kwon H, Yee Y *et al*. Electrostatic MEMS variable optical attenuator with rotating folded micromirror. *IEEE J Sel Top Quant Electron* 2004; **10**: 558–562.
41 Cai H, Zhang XM, Lu C, Liu AQ, Khoo EH. Linear MEMS variable optical attenuator using reflective elliptical mirror. *IEEE Photonic Tech Lett* 2005; **17**: 402–404.
42 Fukuta Y, Fujita H, Toshiyoshi H. Vapor hydrofluoric acid sacrificial release technique for micro electro mechanical systems using labware. *Jpn J Appl Phys* 2003; **42**: 3690–3694.
43 Marcuse D. Loss analysis of single-mode fiber splices. *Bell Syst Tech J* 1977; **56**: 703–718.
44 Goldsmith P. *Quasioptical Systems: Gaussian Beam Quasi-optical Propagation and Applications*. New York: Wiley-IEEE Press; 1997.
45 Zhang QX, Du Y, Tan CW, Zhang J, Yu MB *et al*. A silicon platform with MEMS active alignment function and its potential application in Si-photonics packaging. *IEEE J Sel Top Quant Electron* 2010; **16**: 267–275.
46 Kilic O, Digonnet MJ, Kino GS, Solgaard O. Asymmetrical spectral response in fiber Fabry–Perot interferometers. *IEEE/OSA J Lightw Technol* 2009; **27**: 5648–5656.

This work is licensed under a Creative Commons Attribution-NonCommercial-NoDerivs Works 3.0 Unported license. To view a copy of this license, visit http://creativecommons.org/licenses/by-nc-nd/3.0